

Multilevel approach for the local nanobuckling analysis of CNT-based composites

N. Silvestre*, B. Faria and A. Duarte

Department of Civil Engineering, ICIST, Instituto Superior Técnico, Technical University of Lisbon, Portugal

(Received July, 25, 2012, Revised August 25, 2012, Accepted September 10, 2012)

Abstract. In the present paper, a multilevel approach for the local nanobuckling analysis of carbon nanotube (CNT) based composite materials is proposed and described. The approach comprises four levels, all of them at nanoscale. The first level aims to propose the potential that describes the interatomic forces between carbon atoms. In the second level, molecular dynamics simulations are performed to extract the elastic properties of the CNT. The third level aims to determine the stiffness of the material that surrounds the CNT (matrix), using the annular membrane analysis. In the fourth level, finite strip analysis of the CNT elastically restrained by the matrix is performed to calculate the critical strain at which the CNT buckles locally. In order to achieve accurate results and take the CNT-matrix interaction into account, the 3rd and 4th steps may be repeated iteratively until convergence is achieved. The proposed multilevel approach is applied to several CNTs embedded in a cylindrical representative volume element and illustrated in detail. It shows that (i) the interaction between the CNT and the matrix should be taken into account and (ii) the buckling at nanoscale is sensitive to several types of local buckling modes.

Keywords: carbon nanotube (CNT); composite material; CNT-matrix interaction; molecular dynamics; membrane analysis; finite strip analysis; local buckling

1. Introduction

Carbon nanotubes (CNTs) can be seen as graphene sheets rolled into hollow cylinders composed of hexagonal carbon cells. The hexagonal cell is repeated periodically and binds each carbon atom to three neighboring atoms with covalent bonds, being one of the strongest chemical bonds existing in nature. Therefore, CNTs have impressive mechanical properties. Indeed, a lot of theoretical investigations and few experimental studies were carried out in the last decade, showing that CNTs possess extraordinary mechanical properties (elastic modulus about 1 TPa, tensile strength between 50 and 150 GPa, and failure strain up to 20%). Thus, CNTs offer unique potential for reinforcing standard materials, polymeric, ceramic or metallic, and enhancing the mechanical properties of CNT-based composites. Several works demonstrated their efficiency for reinforcement of material matrices (Qian *et al.* 2000, Wan *et al.* 2005, Desai and Haque 2005, Seidel and Lagoudas 2006, Han and Elliott 2007).

From the point of view of numerical models to extract the mechanical properties, several works

* Corresponding author, Assistant Professor, E-mail: nuno.silvestre@civil.ist.utl.pt

have been published. Kitipornchai *et al.* (2005) derived explicit formulas to describe the buckling behavior of triple-walled CNTs embedded in an elastic matrix. Their investigation was based on the continuum shell theory in which the individual tube is treated as a cylindrical shell and the elastic matrix surrounding the outermost tube is modeled as a Pasternak foundation to account for the normal and shear stresses between the outermost tube and the surrounding matrix. They found that, as the foundation stiffness increases, the critical buckling loads increase quickly at first and then approach a constant value when the stiffness is large enough. With the increase of the innermost radii, the critical buckling load decreases and approaches a constant value, regardless of whether or not the CNT is embedded in an elastic matrix. Using the asymptotic expansion homogenization method and employing a control volume finite element method, Song and Youn (2006) investigated the effective elastic properties of the nanocomposites filled with CNTs. They found that the numerically calculated elastic modulus was in good agreement with that obtained analytically. Tserpes *et al.* (2008) proposed a multiscale representative volume element (RVE) for modeling the tensile behavior of CNT-reinforced composites that integrates nanomechanics and continuum mechanics. They presented a progressive fracture model based on the modified Morse interatomic potential for simulating the behavior of the isolated carbon nanotubes and the FE method for modeling the matrix and building the RVE. Wang *et al.* (2012) studied the flexural buckling of CNTs embedded in an elastic matrix. They modeled CNTs within the framework of Timoshenko beams and used both a stress gradient and a strain gradient approach to obtain the critical buckling loads. They found a significant dependence of critical buckling loads on the nonlocal parameter and the stiffness of the surround matrix.

Despite the existence of several works on the multiscale modeling of CNT-based composites, still there is some lack of knowledge on the influence of CNT local buckling on the mechanical properties of CNT-based composites. It is known that the compressive strength of continuous fiber-reinforced polymer matrix composites is lower than its tensile strength, about one half or less. The

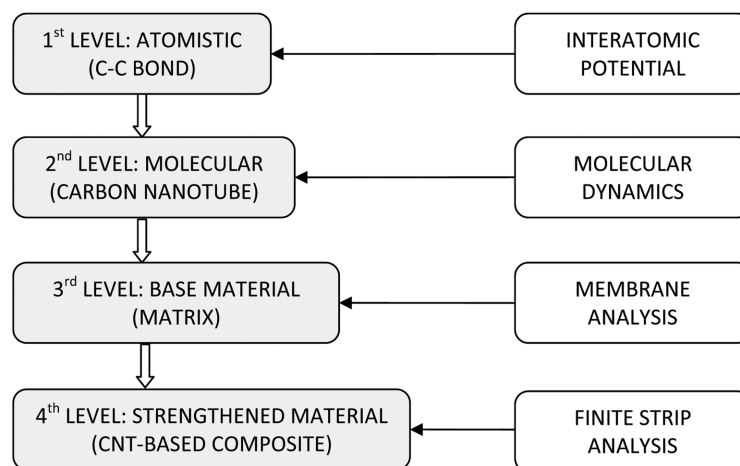


Fig. 1 Flowchart of the multilevel approach

¹This multilevel approach differs from usual multiscale approaches as its steps are solely grounded in nanoscale. However, it is based on several nanoscale levels (atomic bonding, molecular structure, base material, strengthened material).

mode of failure is usually triggered by fiber microbuckling, when individual fibers buckle inside the matrix. Similar phenomena take place at the lower scale (nanoscale) with CNTs. However, since they have a hollow structure (tube), they are prone to buckle either locally or globally. The main objective of this paper is to propose a multilevel approach¹ to study the local buckling of CNTs when embedded in elastic matrices (CNT-based composites). The multilevel methodology aims to evaluate the buckling of CNTs elastically restrained by the matrix and is based in a four-level approach (see Fig. 1):

- 1st level: definition of the C-C bond potential for the analysis of CNT interatomic forces.
- 2nd level: performance of CNT atomistic simulation to estimate its elastic properties.
- 3rd level: execution of plane membrane analysis to estimate the stiffness of the matrix (elastic medium).
- 4th level: performance of finite strip analysis of the CNT taking into account the elastic properties of both CNT and matrix.

2. Atomistic level

The interatomic forces between carbon atoms are described by means of potentials. The present study adopts the AIREBO potential to model the interatomic forces present in the covalent binding of carbon in the CNT structure. This potential is an improved version of Brenner's well-known second generation Reactive Empirical Bond Order Potential (REBO), but includes a Lenhard-Jones potential form to describe the Van-der-Waals long-range interactions (E_{ij}^{LJ}) and a torsional term for the σ -bond torsion ($E_{kijl}^{Torsion}$). The general form for the AIREBO potential is

$$E = \sum_i \sum_{j \neq i} [E_{ij}^{REBO} + \sum_{k \neq i, j} \sum_{l \neq i, j, k} E_{kijl}^{Tors} + E_{ij}^{LJ}] \quad (1)$$

where E_{ij}^{REBO} represents the relation of the short-range interaction force between C atoms in the framework of the second-generation Reactive Empirical Bond Order (REBO) potential, given by

$$E_{ij}^{REBO} = V_{ij}^R(r_{ij}) + b_{ij} V_{ij}^A(r_{ij}) \quad (2)$$

The terms V_{ij}^R and V_{ij}^A are the repulsive and attractive pair potentials, respectively, and b_{ij} is the reactive empirical bond order between atoms. The second term in Eq. (1) is the following torsional potential between carbon atoms.

$$E_{kijl}^{Tors} = \frac{1}{2} w_{ij}(r_{ij}) w_{jk}(r_{jk}) w_{kl}(r_{kl}) \cdot V^{Torsion}(w_{ijkl}) \quad (3)$$

The term $V^{Torsion}(w_{ijkl})$ represents the torsion potential function that simulates the presence of steric barriers between atoms separated by three covalent bonds, and $w_{ij}; w_{jk}; w_{kl}$ are the bound parameters. The last term in Eq. (1) is the non-bonded Lennard-Jones potential, given by

$$E_{ij}^{LJ} = 4\epsilon \left[\left(\frac{\sigma}{r} \right)^{12} - \left(\frac{\sigma}{r} \right)^6 \right] \quad (4)$$

A more detailed description of the AIREBO potential can be found in Stuart *et al.* (2000).

3. Molecular level

The molecular dynamics (MD) simulations were performed using the Large Scale Atomic/Molecular Massively Parallel Simulator (LAMMPS) (Plimpton 1995). The AIREBO potential is included in the LAMMPS software package. The simulation follows a sequence of operations, described next. For a given CNT with radius R and length L , both end sections are located at $x = \pm L/2$ (x is the CNT axis). For extension, incremental displacements are imposed in opposite directions, $\Delta u = -0.025 \text{ \AA}$ for atoms located at $x = -L/2$ and $\Delta u = +0.025 \text{ \AA}$ for atoms located at $x = +L/2$. These imposed displacements stretch the CNT by $\Delta u = 0.050 \text{ \AA}$ in each increment. During the simulations the CNTs are allowed to relax, reaching a new equilibrium state while maintaining the prescribed stretching displacement. All simulations were performed at a temperature of 300 K using the canonical NVT ensemble and Nosé-Hoover thermostat. The newtonian equations of motion were integrated using the velocity-Verlet algorithm. A timestep of 0.8 fs was used and all simulations comprised 10.000 timesteps. The configurational (or strain) energy V of the CNT calculated at the end of each simulation corresponds to the average value of the energy within the last 4.000 timesteps and 400 simulations (increments) were performed in each analysis (Faria *et al.* 2011, Silvestre *et al.* 2012).

In order to extract the Young's modulus of CNTs, we have considered the three types of CNT depicted in Fig. 2(a)

- $(n = 5, m = 5)$ armchair CNT with radius $R = (1.23/\pi)(\sqrt{n^2 + m^2 + nm}) = 3.3 \text{ \AA}$, chiral angle $\theta = \arctg(\sqrt{3}m/2n+m) = 30^\circ$, length $L = 47.3 \text{ \AA}$ and 380 atoms.
- $(n = 8, m = 0)$ zigzag CNT with radius $R = (1.23/\pi)(\sqrt{n^2 + m^2 + nm}) = 3.1 \text{ \AA}$, chiral angle $\theta = \arctg(\sqrt{3}m/2n+m) = 0^\circ$, length $L = 46.3 \text{ \AA}$ and 352 atoms.
- $(n = 6, m = 3)$ chiral CNT with radius $R = (1.23/\pi)(\sqrt{n^2 + m^2 + nm}) = 3.1 \text{ \AA}$, chiral angle $\theta = \arctg(\sqrt{3}m/2n+m) = 19.1^\circ$, length $L = 41.0 \text{ \AA}$ and 336 atoms.

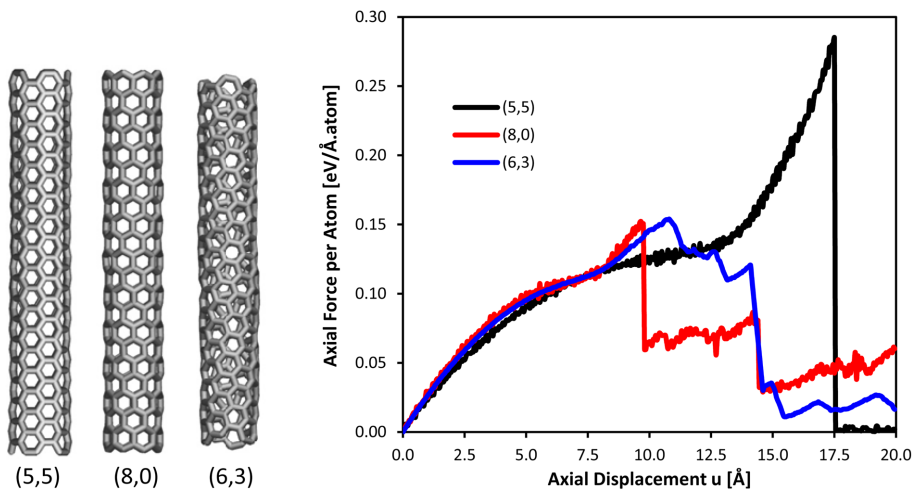


Fig. 2 (a) CNTs adopted in the MD study and (b) force-displacement curves

The three CNTs are single-walled and possess an aspect ratio L/D about 7.0.

The results obtained from the MD simulations are shown in Fig. 2(b), which displays the variation of the force per atom, F , as a function of axial displacement, u (note that $1.0 \text{ eV}/\text{\AA} = 1.602 \text{ nN}$). It is seen that the force varies nonlinearly with the displacement and it drops for a certain amount of displacement. These drops reflect the CNT failure. It is also clear that the three curves show a very similar trend for $0 < u < 8 \text{ \AA}$. However, they become different for increasing axial displacements ($u > 8 \text{ \AA}$) and exhibit different axial displacements at failure. In the present study, we are only interested in the elastic properties. Thus, we limit our analysis to low axial displacements ($0 < u < 3 \text{ \AA}$). In this range, F varies linearly with u . By fitting a linear regression to the $F(u)$ curve in the range $0 < u < 3 \text{ \AA}$, we obtain the following derivatives

$$\cdot (n = 5, m = 5) \text{ armchair CNT: } (\partial F/\partial u) = 0.0206 \text{ eV}/\text{\AA}^2 \quad (5)$$

$$\cdot (n = 8, m = 0) \text{ zigzag CNT: } (\partial F/\partial u) = 0.0247 \text{ eV}/\text{\AA}^2 \quad (6)$$

$$\cdot (n = 6, m = 3) \text{ chiral CNT: } (\partial F/\partial u) = 0.0234 \text{ eV}/\text{\AA}^2 \quad (7)$$

which are very similar, with an average of $0.0229 \text{ eV}/\text{\AA}^2$ and a standard deviation equal to $0.002 \text{ eV}/\text{\AA}^2$. From these data, it is also possible to evaluate the Young's modulus from the slope of the $F(u)$ linear path, using $Y = (\partial F/\partial u)(L/2\pi Rh)$, where h is the CNT thickness (we have considered $h = 3.4 \text{ \AA}$)

$$\cdot (n = 5, m = 5) \text{ armchair CNT: } Y = 0.75 \text{ TPa} \quad (8)$$

$$\cdot (n = 8, m = 0) \text{ zigzag CNT: } Y = 0.93 \text{ TPa} \quad (9)$$

$$\cdot (n = 6, m = 3) \text{ chiral CNT: } Y = 0.78 \text{ TPa} \quad (10)$$

The obtained Y values agree with the 0.77 TPa and 0.82 TPa values obtained by Agrawal *et al.* (2006) and Talukdar and Mitra (2010), respectively, using MD simulations with a similar value of CNT thickness. Cooper and Young (2000) measured experimentally the Young's modulus of single-walled CNTs using Raman spectroscopy and obtained minimum values around 0.78 TPa, matching the lower Y values found in this study. Moreover, Leung *et al.* (2006) found Y values between 0.80 and 1.0 TPa. The Young's modulus of CNTs is usually taken as 1.0 TPa, but smaller values take place for CNTs with decreasing radius. In this study, we will consider a mean value of $Y = 0.90 \text{ TPa} = 9.0 \text{ nN}/\text{\AA}^2$.

4. Base material level

In order to move to the upper scale, it is necessary to consider a representative volume element

²One issue that remains less clear concerns the value of CNT thickness. It is known that graphene (CNT wall) possess a membrane stiffness $C = Eh = 360 \text{ J/m}^2$, thus it is possible to adopt thickness values from $h = 3.40 \text{ \AA}$ to $h = 0.66 \text{ \AA}$, or any other h value that satisfy $Eh = 3.60 \text{ TPa \AA}$. The first option has a clear physical meaning, since $h = 3.40 \text{ \AA}$ is the equilibrium interlayer spacing of adjacent CNTs. In this specific analysis, we adopt $h = 3.4 \text{ \AA}$.

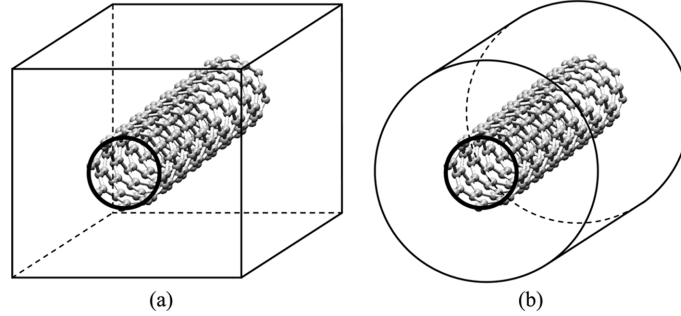


Fig. 3 RVEs of the CNT-based composite: (a) quadrangular and (b) circular

(RVE), which comprises the CNT and the matrix (elastic medium). Generally, the RVE is a tri-dimensional cell that replicates the behaviour of the composite material and it is repeated many times to reproduce the medium. Fig. 3 shows two usual RVE's, a quadrangular prism (Fig. 3(a)) and a cylinder (Fig. 3(b)). In the present paper, we selected the cylindrical RVE (Fig. 3(b)). The mechanical behaviour of the RVE (nano-composite material) is determined in two steps. The first step is to determine the contribution of the matrix to restrain the deformation of the CNT. If we assume the elastic properties of the matrix are known, the stiffness of the elastic medium can be assessed by resorting to a plane membrane analysis.

Let us consider a circular annular membrane representative of the matrix around the CNT. The stress state is considered bi-dimensional and the equilibrium differential equation given by the Reissner theory reads

$$\rho^2 \frac{\partial^2 u}{\partial \rho^2} + \rho \frac{\partial u}{\partial \rho} - u = -\rho^2 \frac{pR_e}{Eh/(1-\nu^2)} \quad (11)$$

Where $\rho = r/R_e$, $u = U/R_e$. In this equation, r is the radial coordinate of an arbitrary point with respect to the centre of the annular flat membrane, U is the radial displacement of that point, R_e is the outer radius of the circular annular membrane (i.e., the radius of the cylindrical RVE), p is a radial distributed load and $Eh/(1-\nu^2)$ is the membrane equivalent stiffness of the matrix. The radial σ_{rr} and circumferential $\sigma_{\theta\theta}$ stresses are given by

$$\sigma_{rr} = \left(\frac{\partial u}{\partial \rho} + \nu \frac{u}{\rho} \right) \frac{E}{(1-\nu^2)} \quad (12)$$

$$\sigma_{\theta\theta} = \left(\frac{u}{\rho} + \nu \frac{\partial u}{\partial \rho} \right) \frac{E}{(1-\nu^2)} \quad (13)$$

If we consider the simplest case, i.e., axi-symmetric displacement A of the inner boundary of the annular membrane (interface CNT-matrix), an analytical solution exists and it is given by

$$u = -A \frac{R_i}{R_e} \frac{1-\rho^2}{\rho \left(1 - \frac{R_i}{R_e}\right)} \quad (14)$$

$$\sigma_{rr} = AE \frac{R_i(1+\nu)\rho^2 + (1-\nu)}{R_e(1-\nu^2)\left(1 - \frac{R_i^2}{R_e^2}\right)\rho^2} \quad (15)$$

$$\sigma_{\theta\theta} = AE \frac{R_i(1+\nu)\rho^2 - (1-\nu)}{R_e(1-\nu^2)\left(1 - \frac{R_i^2}{R_e^2}\right)\rho^2} \quad (16)$$

However, axi-symmetric deformation is not the usual case. In fact, local buckling of CNTs occurs for two or multiple wrinkles (lobes) along their cross-section contour. Thus, it is necessary to determine the stiffness of the circular annular membrane when a point of its inner contour is acted by (i) a radial load, (ii) a tangential load, (iii) a moment perpendicular to the membrane plane. In this case, the number of terms in Eq. (11) increases because the displacement v in the circumferential direction comes into play and an additional differential equation appears. The problem can be solved by using Fourier series for (u, v) in the plane (r, θ) . Fig. 4 shows the solution obtained for the von Mises stress distributions (function of σ_{rr} , $\sigma_{\theta\theta}$, $\tau_{r\theta}$) in the vicinity of point P located at the inner boundary and acted by a radial load, tangential load, and moment perpendicular to the membrane plane. Fig. 5 shows the solution obtained for the total displacement $\sqrt{u^2 + v^2}$, corresponding to the application of radial load, tangential load and a moment.

Fig. 4 shows that the isoline displacement diagrams have different shapes for radial and tangential

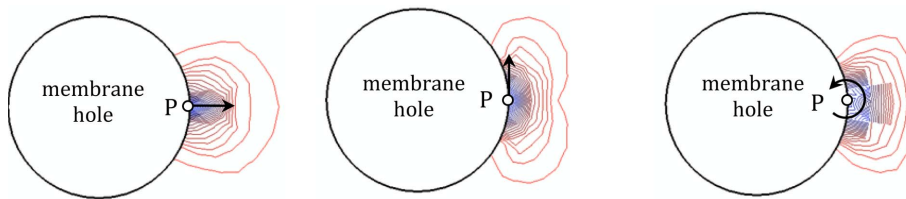


Fig. 4 Displacements distributions due to the imposition of forces

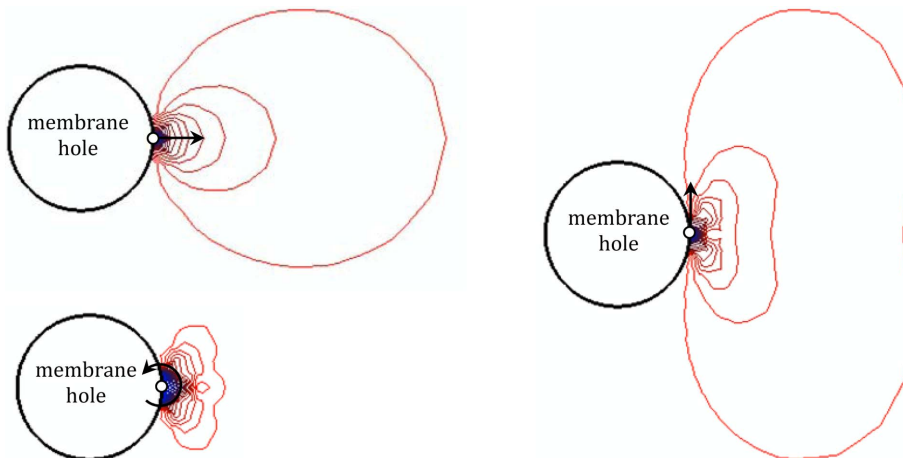


Fig. 5 Stress distributions due to the imposition of forces

forces, the first being more spread in the radial direction while the second being more extended along the circumferential direction of the hole. Regarding the applied moment diagram, its shape is somewhere between those diagrams of radial and tangential forces. Fig. 5 shows that the isoline stress diagrams are very different. For radial and tangential forces, the diagrams have ovalized shapes in the radial and tangential directions, respectively. In the case of the applied moment diagram, the stress isolines become highly localized and close to the point P . From this study, we conclude that the influence of rotational stiffness due to the applied moment is less influential than the stiffness due to the radial and tangential forces.

Using the solutions obtained before, we determined the stiffness around the CNT hole due to radial and tangential forces. In this study, we considered a polymeric matrix ($E = 5 \text{ GPa} = 0.05 \text{ nN}/\text{\AA}^2$ and $\nu = 0.2$) and we varied the area of the membrane by means of the adoption of three different external radius ($R_e = 25 \text{ \AA}$, $R_e = 50 \text{ \AA}$, $R_e = 100 \text{ \AA}$). In each case, we varied the CNT radius from a minimum of $R_i = 3.4 \text{ \AA}$ to a maximum of $R_i = 13.6 \text{ \AA}$. This task was done by varying the chiral indices n and m from 5 to 20, by intervals of 5. Figs. 6 and 7 show the variation of radial stiffness (K_{rad}) and tangential stiffness (K_{tan}) with the CNT hole radius R_i . It is clearly seen that the dimension of the RVE (membrane radius) has a great impact on the stiffnesses, either radial or tangential. The stiffness values remain almost unchanged with R_i for $R_e = 100 \text{ \AA}$, while they vary a lot with R_i for $R_e = 25 \text{ \AA}$. For $R_e = 50 \text{ \AA}$, a small variation exists. It is also clear that the variation is more evident for the radial stiffness (K_{rad} – Fig. 6) than for the tangential one (K_{tan} – Fig. 7).

We also concluded that the stiffness does not depend directly on the R_i and R_e values but rather on their ratio (R_i/R_e). For instance, see the black circles in Figs. 6 and 7, which correspond to ($R_e = 25 \text{ \AA}$, $R_i = 6.8 \text{ \AA}$) and ($R_e = 50 \text{ \AA}$, $R_i = 13.6 \text{ \AA}$). They have different R_i and R_e values but they have equal ratio $R_i/R_e = 0.272$. A similar trend occurs for other radius values. Thus it is possible to plot single curves not depending on the radius values but rather on the ratio R_i/R_e or any dependent variable. Thus, we define the fraction of the RVE area occupied by the CNT as $A_f = A_i/A_e = (R_i/R_e)^2$, which depends solely on the ratio R_i/R_e .

Fig. 8 shows the variation of the radial and tangential stiffness with the area fraction A_f (in

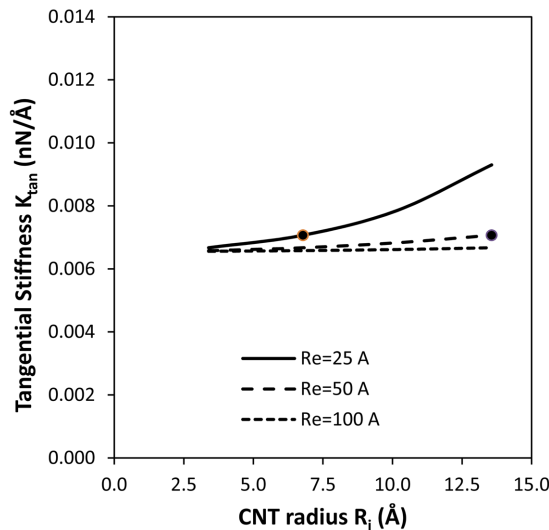


Fig. 6 Variation of radial stiffness with the CNT radius R_i and RVE radius R_e

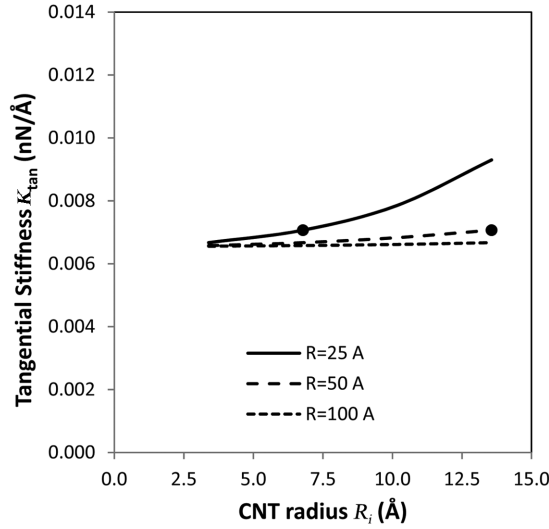


Fig. 7 Variation of tangential stiffness with the CNT radius R_i and RVE radius R_e

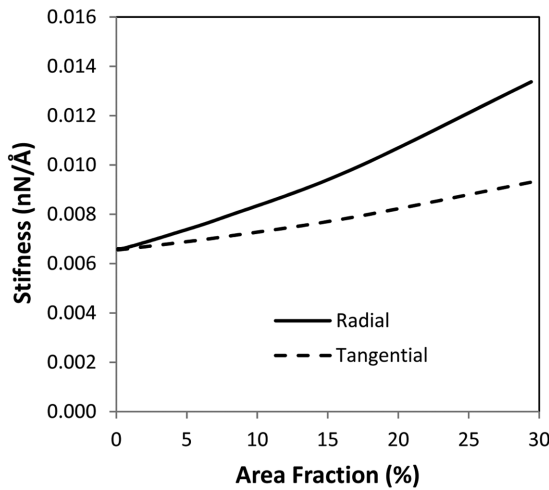


Fig. 8 Variation of radial and tangential stiffness with the CNT area fraction

percentage). Since both $K_{rad}(A_f)$ and $K_{tan}(A_f)$ curves tend to the same value for $A_f = 0$, i.e., $K_{rad} = K_{tan} = 0.0065 \text{ nN/Å}$, the consistency of the current analysis becomes obvious - note that $A_f = 0$ means that no hole exists and uniform and continuous medium exists, thus implying the equality between radial and tangential stiffness. Furthermore, it is possible to fit the best exponential regression to the data. With a correlation factor of $\rho = 0.999$, this gives the following general expression,

$$K = 0.0065 e^{\gamma A_f} \tag{17}$$

³Recall that the value $K = 0.0065 \text{ nN/Å}$ was obtained for $E = 5 \text{ GPa} = 0.05 \text{ nN/Å}^2$ and $\nu = 0.2$. For other matrix modulus values, a linear interpolation might be applied.

where $\gamma = 0.0242$ and $\gamma = 0.0118$ stand for the radial and tangential stiffness, respectively³.

5. Strengthened material level

Having obtained (i) the Young's modulus of the CNT (2nd level) and (ii) the variation of radial and tangential stiffness of the matrix with the CNT and RVE radius values (3rd level), we are able to perform the last step of this multilevel approach, which is the determination of the local buckling strains of the CNT-based composite. For this step, we apply the Semi-Analytical Finite Strip Method (CUFSM 2006) to perform the buckling analysis of the CNT elastically restrained by the matrix, where the elastic medium is simulated by means of a Pasternak foundation model. We consider four single-walled CNTs ((5,5), (10,10), (15,15) and (20,20)) with the following properties: $Y = 0.9 \text{ TPa} = 9.0 \text{ nN/\AA}^2$, $\nu = 0.2$. We model the CNTs as elastic shells with thickness $h = 0.70 \text{ \AA}^4$ and the circular cross-section discretized with 40 strips.

Fig. 9 shows the variation of buckling strain ε_b with the buckling half-wavelength L of the CNT, for an RVE with $R_e = 100 \text{ \AA}$. This Figure shows that the four $\varepsilon_b(L)$ curves have local minima that correspond to the critical strain values $\varepsilon_{cr} = 0.089$ (5,5), $\varepsilon_{cr} = 0.058$ (10,10), $\varepsilon_{cr} = 0.042$ (15,15), $\varepsilon_{cr} = 0.033$ (20,20). It is very interesting to note that these critical strains always take place for a single critical half-wavelength $L = 7.0 \text{ \AA}$, regardless of the CNT radius. This means that the CNT will buckle with longitudinal waves around 14 \AA . We can also observe that the critical strain decreases

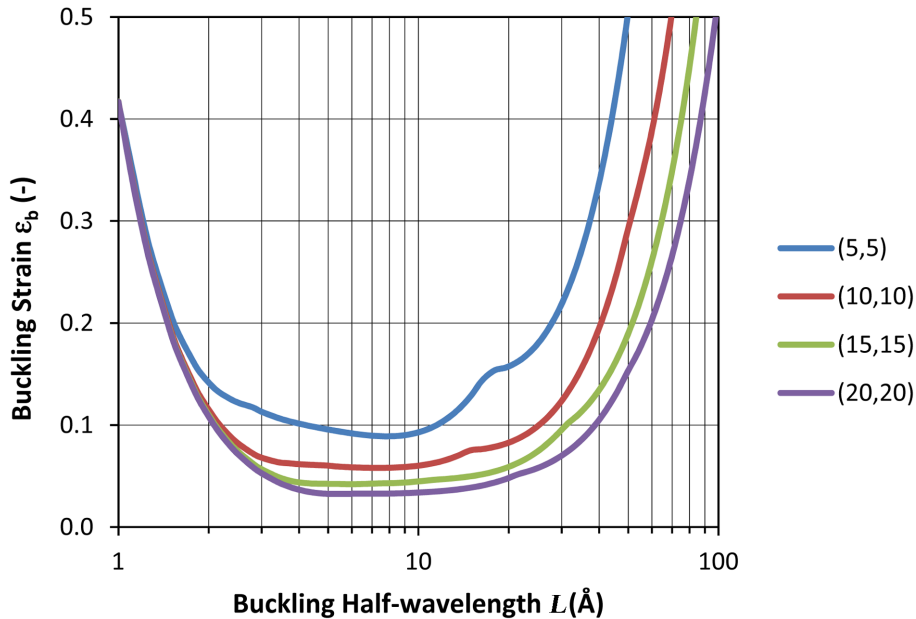


Fig. 9 Variation of CNT buckling strain with the half-wavelength L (RVE with $R_e = 100 \text{ \AA}$)

⁴The CNT thickness to use in shell models also remains unknown. The value $h = 0.66 \text{ \AA}$, proposed by Yakobson *et al.* (1996) has been widely used since it gives better results in CNT analysis using shell models. Herein, we adopte $h = 0.70 \text{ \AA}$, a value that is close to $h = 0.66 \text{ \AA}$, $h = 0.73 \text{ \AA}$, and $h = 0.76 \text{ \AA}$, values proposed by Yakobson *et al.* (1996), Huang *et al.* (2006) and Wang *et al.* (2008).

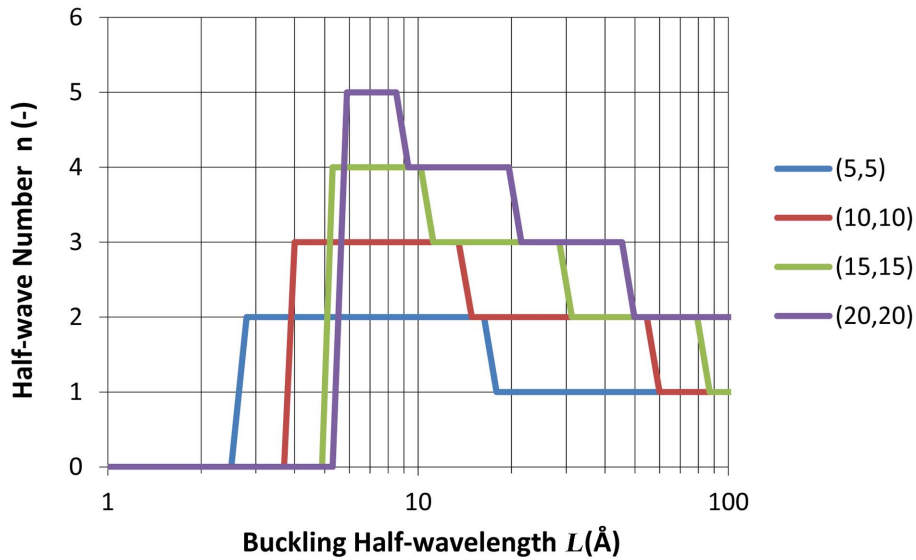


Fig. 10 Variation of half-wave number n with the CNT half-wavelength L (RVE with $R_e = 100 \text{ \AA}$)

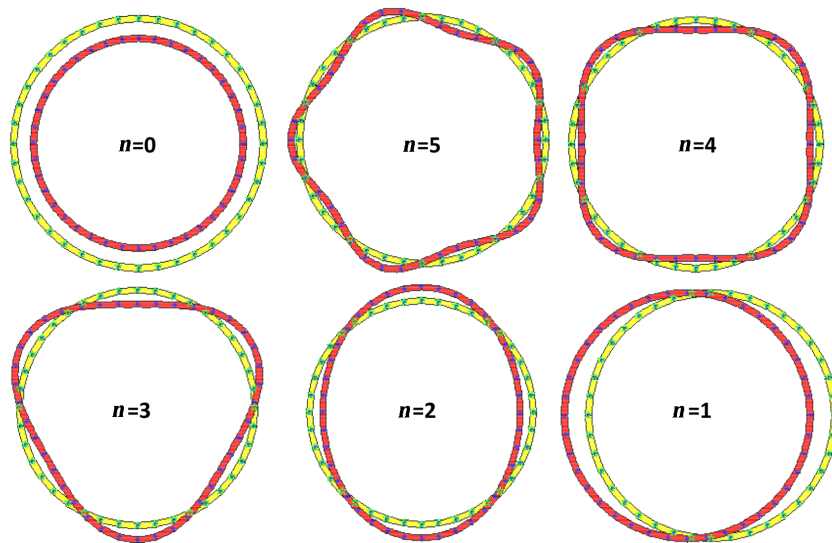


Fig. 11 Buckling mode shapes (in-plane displacements u and v) varying with the circumferential half-wave number n

with increasing radius. More interesting than this fact is the change in shape of the $\varepsilon_b(L)$ curve: the bottom zone of the $\varepsilon_b(L)$ curve tends to form a horizontal plateau as the CNT radius increases, from (5,5) to (20,20). In order to explain such a behaviour, we must introduce Fig. 10, which depicts the variation of the circumferential half-wave number n with the CNT half-wavelength L (RVE with $R_e = 100 \text{ \AA}$) - the nodal in-plane displacements shown in this figure correspond to the radial u and tangential v displacements defined before in section 4. From this figure, we observe that the CNT buckling mode shape varies much more for increasing CNT radius. For instance, the (5,5) CNT

shows three buckling mode shapes, with $n = 0$ (axi-symmetric mode), $n = 2$ (ovalization mode) and $n = 1$ (bending mode) - these shapes are drawn in Fig. 11. In the opposite side, the (20,20) CNT shows five buckling mode shapes: besides the modes with $n = 0$ (axi-symmetric mode) and $n = 2$ (ovalization mode), it also exhibits the buckling mode shapes with $n = 5$, $n = 4$ and $n = 3$ (see Fig. 11). Furthermore, we also observe that axi-symmetric buckling mode ($n = 0$) becomes more preminent as the CNT radius increases. The cumulative effect of (i) increasing radius, (ii) higher number of modes and (iii) wider length range for axi-symmetric buckling, imply the augmented horizontal plateau exhibited by the bottom zone of the $\varepsilon_b(L)$ curves shown in Fig. 9. From Figs. 10 and 11, it

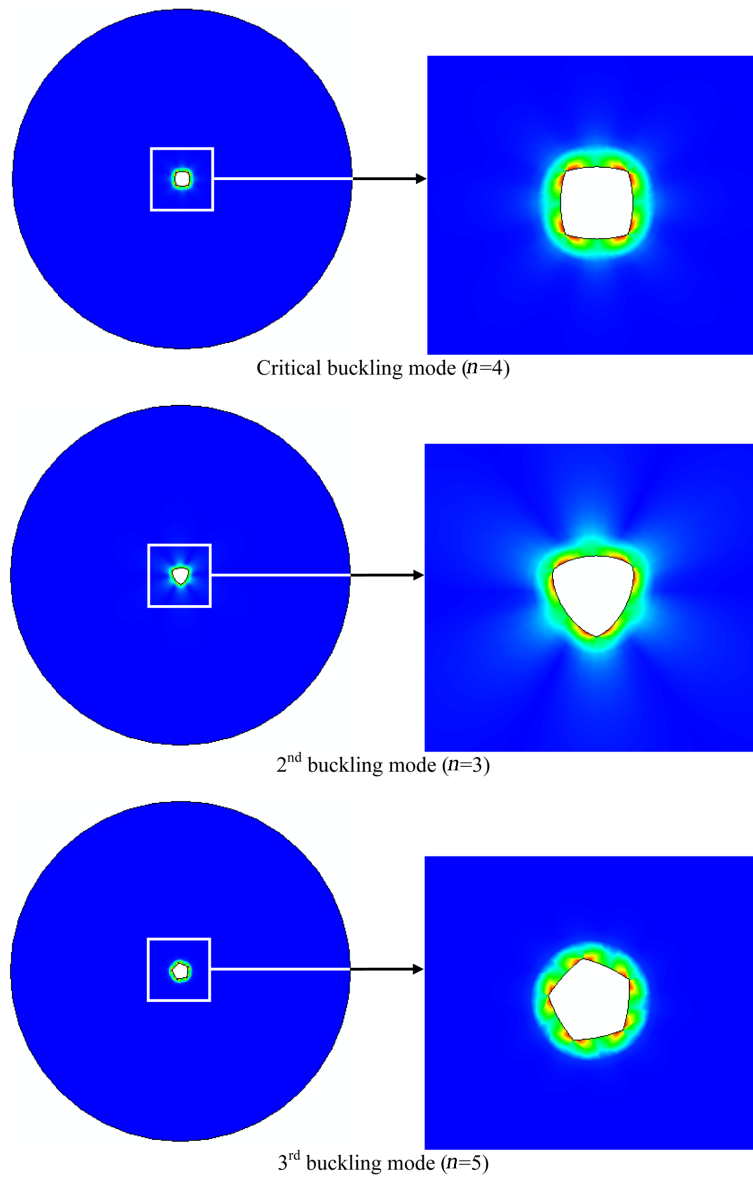


Fig. 12(a) Critical, 2nd and 3rd buckling mode shapes of CNT-based composite RVE

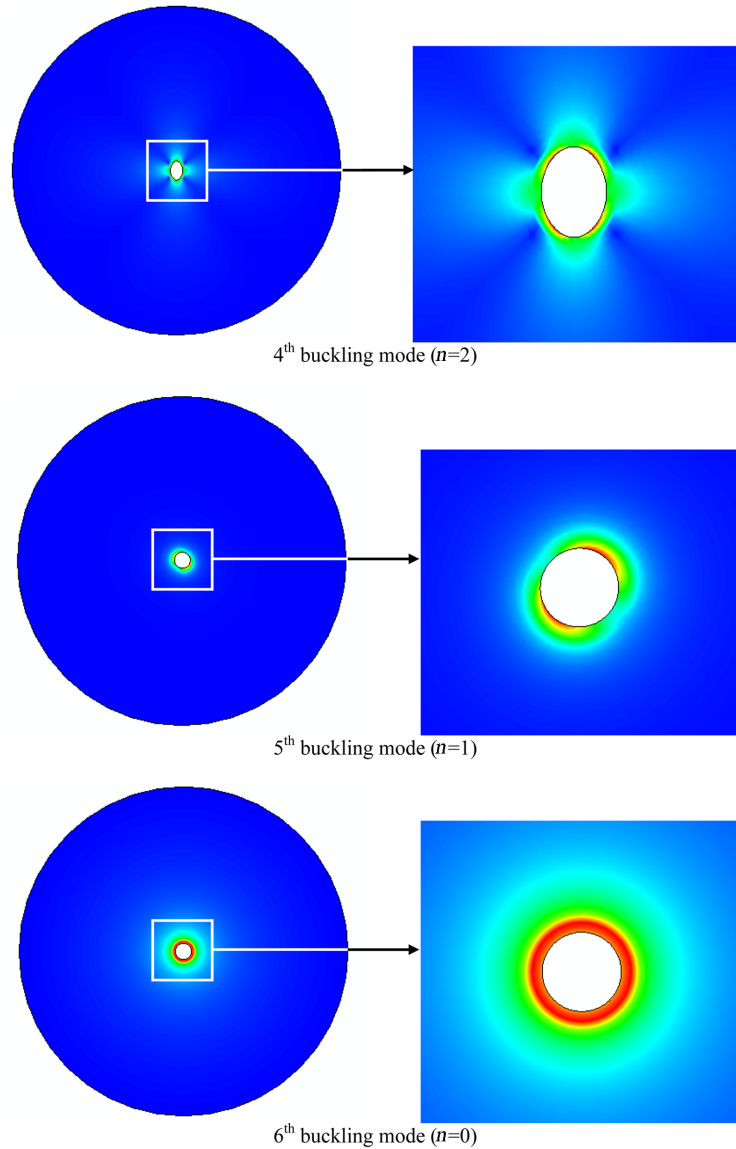


Fig. 12(b) 4th, 5th and 6th buckling mode shapes of CNT-based composite RVE

is also possible to see that the critical mode, corresponding to $L = 7.0 \text{ \AA}$, varies with the CNT radius: (i) $n = 2$ for (5,5), (ii) $n = 3$ for (10,10), (iii) $n = 4$ for (15,15) and (iv) $n = 5$ for (20,20).

Within the scope of the multilevel methodology presented in this paper, it is also possible (i) to couple the finite strip buckling analysis with the annular membrane analysis and (ii) to develop an interactive approach to study the mechanical (elastic) behaviour of CNT-based composites. This methodology takes the CNT-matrix interaction into account in a more rigorous way, as the exact radial and tangential stiffness values are derived for the specific local buckling mode. The approach has an iterative nature and follows the following steps:

- (i) Determination of the CNT Young's modulus based on tensile virtual tests performed via

molecular dynamics simulations (2nd level).

(ii) Determination of the matrix radial and tangential stiffness (K_{rad} and K_{tan}) based on annular membrane analysis (3rd level).

(iii) Calculation of the CNT buckling strain (ε_b) and buckling mode shape (in-plane displacements u and v) from finite strip analysis, taking into account the CNT and matrix properties defined in steps (i) and (ii).

(iv) Imposition of the buckling mode shapes (in-plane displacements u and v) to the annular membrane and determination of the corresponding CNT-matrix modal stiffness values (K_{rad} and K_{tan}).

(v) Iteration of steps (iii) and (iv) until convergence is achieved for the buckling strain (ε_b value - usually, only few (two or three) steps are required).

The approach was applied to a RVE with external radius $R_e = 150 \text{ \AA}$, and incorporating a (20,20) CNT with radius $R_i = 13.6 \text{ \AA}$ and length $L = 100 \text{ \AA}$. The buckling strain ε_b values varied from 0.032 (1st iteration) to 0.028 (3rd and last iteration). In the longitudinal direction, the CNT buckles into 14 half-waves. The in-plane shapes (u and v) of the first 6 buckling modes of the CNT-based composite RVE are shown in Figs. 12(a) and (b). The von Mises stress state diagrams in the matrix are also shown in colour. It is seen that the critical buckling mode is the 4-lobe mode ($n = 4$). The remaining 5 buckling modes are those corresponding to $n = 3$ (2nd mode - Fig. 12(a)), $n = 5$ (3rd mode - Fig. 12(a)), $n = 2$ (4th mode - Fig. 12(b)), $n = 1$ (5th mode - Fig. 12(b)) and $n = 0$ (6th mode - Fig. 12(b)). From the observation of Fig. 12, we conclude that the CNT axi-symmetric buckling mode ($n = 0$) induces the highest stress amplitudes in the matrix and stress concentration becomes higher with increasing number of buckling mode lobes. Finally, we also conclude that the CNT buckling mode shapes obtained from this iterative approach do not differ much from the buckling mode shapes obtained in the first iteration, qualitatively represented in Fig. 11.

6. Conclusions

A nanoscale 4-level approach for the local nanobuckling analysis of CNT-based composites was proposed and explained in this paper. The first level aimed to propose the potential simulating the C-C interatomic forces. The second level comprised molecular dynamics simulations for the determination of CNT elastic properties. The third level aimed to explain the annular membrane analysis for the determination of the stiffness of matrix surrounding the CNT. The fourth level described the performance of finite strip analysis of the CNT elastically restrained by the matrix and the calculation of the CNT critical strains and local buckling modes. In order to take the CNT-matrix into account and to achieve accurate results, the last two steps were repeated iteratively until critical strain convergence was achieved. The proposed multilevel approach was applied and illustrated in detail for several CNTs ((5,5), (10,10), (15,15), (20,20)) embedded in a cylindrical representative volume element. It was shown that (i) the interaction between the CNT and the matrix should be taken into account and (ii) the buckling at nanoscale might be sensitive to several types of local buckling modes.

Acknowledgements

The authors gratefully acknowledge the financial support given by FCT, in the context of the

project “Modelling and Analysis of Nanostructures: Carbon Nanotubes and Nanocomposites” (PTDC/ECM/103490/2008).

References

- Agrawal, P.M., Sudalayandi, B.S., Raff, L.M. and Komanduri, R. (2006), “A comparison of different methods of Young’s modulus determination for single-wall carbon nanotubes (SWCNT) using molecular dynamics (MD) simulations”, *Comput. Mater. Sci.*, **38**(2), 271-281.
- Cooper, C.A. and Young, R.J. (2000), “Investigation into the deformation of carbon nanotubes and their composites through the use of Raman spectroscopy”, *Proceedings of the SPIE - Optical Devices and Diagnostics in Materials Science*, 4098.
- CUFSM (2006), *Elastic buckling analysis of thin-walled members by finite strip analysis*, CUFSM v3.12. Available from <http://www.ce.jhu.edu/bschafer>
- Desai, A.V. and Haque, M.A. (2005), “Mechanics of the interface for carbon nanotube-polymer composites”, *Thin Wall Struct.*, **43**(11), 1787-1803.
- Faria, B., Silvestre, N. and Canongia Lopes, J.N. (2011), “Interaction diagrams for carbon nanotubes under combined shortening-twisting”, *Compos. Sci. Technol.*, **71**(16), 1811-1818.
- Han, Y. and Elliott, J. (2007), “Molecular dynamics simulations of the elastic properties of polymer/carbon nanotube composites”, *Comput. Mater. Sci.*, **39**(2), 315-323.
- Huang, Y., Wu, J. and Hwang, K.C. (2006), “Thickness of graphene and single-wall carbon nanotubes”, *Phys. Rev. B*, **74**(24), 245413-9.
- Kitipornchai, S., He, X.Q. and Liew, K.M. (2005), “Buckling analysis of triple-walled carbon nanotubes embedded in an elastic matrix”, *J. Appl. Phys.*, **97**(11), 114318.
- Leung, A.Y.T., Wu, Y.D. and Zhong, W.F. (2006), “Computation of Young’s moduli for chiral single-walled carbon nanotubes”, *Appl. Phys. Lett.*, **88**, 251908.
- Plimpton, S. (1995), “Fast parallel algorithms for short-range molecular dynamics”, *J. Comput. Phys.*, **117**, 1-19.
- Qian, D., Dickey, E., Andrews, R. and Rantell, T. (2000), “Load transfer and deformation mechanisms in carbon nanotube-polystyrene composites”, *Appl. Phys. Lett.*, **76**(20), 2868-2870.
- Seidel, G.D. and Lagoudas, D.C. (2006), “Micromechanical analysis of the effective elastic properties of carbon nanotube reinforced composites”, *Mech. Mater.*, **38**(8-10), 884-907.
- Silvestre, N., Faria, B. and Canongia Lopes, J.N. (2012), “A Molecular dynamics study on the thickness and postcritical strength of carbon nanotubes”, *Compos. Struct.*, **94**(4), 1352-1358.
- Song, Y.S. and Youn, J.R. (2006), “Modeling of effective elastic properties for polymer based carbon nanotube composites”, *Polymer*, **47**(5), 1741-1748.
- Stuart, S., Tutein, A.B. and Harrison, J.A. (2000), “A reactive potential for hydrocarbons with intermolecular interactions”, *J. Chem. Phys.*, **112**, 6472-6486.
- Talukdar, K. and Mitra, A.K. (2010), “Influence of odd and even number of stone-wales defects on the fracture behaviour of an armchair single-walled carbon nanotube under axial and torsional strain”, *Molecular Simulation*, **36**(6), 409-417.
- Tserpes, K.I., Papanikos, P., Labeas, G. and Pantelakis, Sp.G. (2008), “Multi-scale modeling of tensile behavior of carbon nanotube-reinforced composites”, *Theor. Appl. Fract. Mec.*, **49**(1), 51-60.
- Wan, H., Delale, F. and Shen, L. (2005), “Effect of CNT length and CNT-matrix interphase in carbon nanotube (CNT) reinforced composites”, *Mech. Res. Commun.*, **32**(5), 481-489.
- Wang, B.L., Hoffman, M. and Yu, A.B. (2012), “Buckling analysis of embedded nanotubes using gradient continuum theory”, *Mech. Mater.*, **45**, 52-60.
- Wang, Q., Liew, K.M. and Duan, W.H. (2008), “Modeling of the mechanical instability of carbon nanotubes”, *Carbon*, **46**(2), 285-290.
- Yakobson, B.I., Brabec, C.J. and Bernholc, J. (1996), “Nanomechanics of carbon tubes: instabilities beyond linear response”, *Phys. Rev. Lett.*, **76**(14), 2511-2514.